Identification of divacancy and silicon vacancy qubits in 6H-SiC

View Online   Export Citation   CrossMark

Joel Davidsson,[1,a] [iD] Viktor Ivády,[1,2] [iD] Rickard Armiento,[1] [iD] Takeshi Ohshima,[3] [iD] N. T. Son,[1] [iD] Adam Gali,[2,4] [iD]
and Igor A. Abrikosov[1,5]

AFFILIATIONS

[1]Department of Physics, Chemistry and Biology, Linköping University, SE-581 83 Linköping, Sweden
[2]Wigner Research Centre for Physics, Hungarian Academy of Sciences, PO Box 49, H-1525 Budapest, Hungary
[3]National Institutes for Quantum and Radiological Science and Technology, 1233 Watanuki, Takasaki, Gunma 370-1292, Japan
[4]Department of Atomic Physics, Budapest University of Technology and Economics, Budafoki út 8., H-1111 Budapest, Hungary
[5]Materials Modeling and Development Laboratory, National University of Science and Technology 'MISIS', 119049 Moscow, Russia

[a]Electronic mail: joel.davidsson@liu.se

ABSTRACT

Point defects in semiconductors are relevant for use in quantum technologies as room temperature qubits and single photon emitters. Among suggested defects for these applications are the negatively charged silicon vacancy and the neutral divacancy in SiC. The possible nonequivalent configurations of these defects have been identified in 4H-SiC, but for 6H-SiC, the work is still in progress. In this paper, we identify the different configurations of the silicon vacancy and the divacancy defects to each of the V1-V3 and the QL1-QL6 color centers in 6H-SiC, respectively. We accomplish this by comparing the results from *ab initio* calculations with experimental measurements for the zero-phonon line, hyperfine tensor, and zero-field splitting.

Published under license by AIP Publishing. https://doi.org/10.1063/1.5083031

In recent years, point defects in semiconductors have been suggested for implementing quantum bits (qubits)[1–3] and single photon sources[4–8] for quantum computation,[9] quantum information processing,[10] spintronics,[3] and quantum sensing applications.[11–13] The most studied point defect qubits are the negatively charged nitrogen-vacancy center (NV center) in diamond,[1,14] the neutral divacancy in SiC,[15,16] and the negatively charged silicon vacancy in SiC.[17,18] All these defects exhibit well isolated electron spin states with long coherence time and operate even at room temperature.[18–20] SiC is a technologically mature host for qubits and single photon emitters, which makes it possible to integrate quantum technologies and semiconductor devices. There are numerous polytypes of SiC which often host multiple symmetrically non-equivalent Si and C sites in their primitive cell. Consequently, point defect qubits may have several nonequivalent configurations with different characteristics in each polytype which provide alternative tools for engineering qubit properties in SiC.[16] Assigning the experimental photoluminescence (PL) and electron spin resonance (ESR) signals to the nonequivalent configurations is indispensable for deeper understanding of the qubits. Recently, several studies have been published on the identification of the microscopic structure of point defect qubits in 4H-SiC.[21–23]

4H and 6H polytypes are the most commonly used hexagonal polytypes of SiC with wafer size samples and high quality. For 6H-SiC, there are 12 atoms in the primitive cell with 3 non-equivalent sites for both species, see Fig. 1(a). Considering only the immediate vicinity of the sites, one site has a hexagonal-like environment, while the other two sites have cubic-like environments. These sites are commonly labeled as h, $k1$, and $k2$ [see Fig. 1(a)], respectively. In general, 6H-SiC gives rise to 3 configurations for single site point defects, such as the silicon vacancy, and 6 configurations for pair defects, such as the divacancy. For the silicon vacancy, the configurations are named h, $k1$, and $k2$, all of which have C_{3v} point group symmetry. The related photoluminescence (PL) signals are referred to as V1-V3[24] centers. Optically detected magnetic resonance (ODMR) and electron paramagnetic resonance (EPR) centers are referred to as T_{V1a}-T_{V3a} centers[24] and $V_{Si}^-(I) - V_{Si}^-(II)$ centers.[25] For the divacancy, we use the notation V_{Si}-V_C, and thus, the following configurations are possible: hh, $k1k1$, and $k2k2$ with C_{3v} point group symmetry and $hk2$, $k1h$, and $k2k1$ with C_{1h} point group symmetry. Divacancy defects in 6H-SiC give rise to the QL1-QL6[16] PL and P6-P7 ESR centers,[26] respectively. The symmetry arguments for the divacancy and silicon vacancy in 6H-SiC are the same as those in 4H-SiC.[27,28]
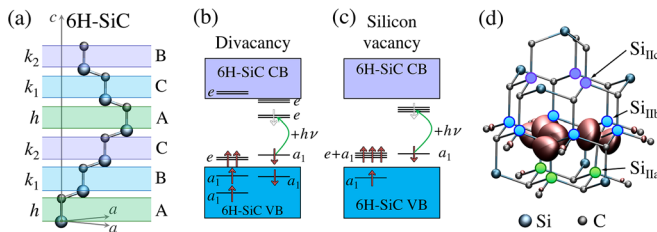
FIG. 1. (a) depicts the primitive cell of 6H-SiC. Light green, light blue, and light purple bands highlight the hexagonal-like (h) and the two different cubic-like ($k1$ and $k2$) Si-C double layers. (b) and (c) depict a schematic diagram of the Kohn-Sham electronic structure of the neutral divacancy and the negatively charged silicon vacancy, respectively. CB stands for the conduction band and VB for the valance band. Green arrows represent the optical absorption processes that drive the defects into their lowest energy optically excited state. (d) Configuration and spin density of the hh divacancy. ^{29}Si sites considered in the hyperfine tensor calculations are marked with colored circles.

The theoretical description and engineering of the defect centers require the assignment of each of the different microscopic configurations. This has been done for the silicon vacancy[22] and the divacancy in 4H-SiC,[21,23,27] but for 6H-SiC, the work is still in progress. In this paper, we present an accurate identification of the different configurations for the divacancy and silicon vacancy point defects in 6H-SiC. To assign the different configurations, we use the approach of comparing experimental measurements with first-principles theoretical calculations. The properties used for this comparison are the zero-phonon line (ZPL) energy, the zero-field splitting (ZFS) parameter, and hyperfine splitting due to the first and second neighbor nuclear spins.

To calculate the ZPL, ZFS, and hyperfine parameters, we employ the density functional theory[29–31] (DFT). The calculations are performed by using the Vienna Ab initio Simulation Package (VASP),[32,33] which uses the projector augmented wave (PAW) method[34,35] for core electrons and the plane wave basis set for valence electrons. For exchange-correlation, we use the semi-local functional of Perdew, Ernzerhof, and Burke (PBE)[36] and the non-local range-separated hybrid functional of Heyd, Scuseria, and Ernzerhof (HSE06).[37,38]

The calculations with the PBE functional are carried out with a plane wave energy and a kinetic energy cutoff of 420 eV and 840 eV, respectively. The energy criteria for the self-consistent cycle and the structural relaxation are set to 10^{-5} eV and 10^{-3} eV, respectively. For the HSE functional calculations, the plane wave energy and kinetic energy cutoff are the same as for the PBE functional. The energy convergence criterion is lowered to 10^{-4} eV. For the hybrid functional computations, the grid for the Fast Fourier Transformation (FFT) for the semi-local exchange is set to twice the largest wave vector, and for the exact exchange, it is set to the largest wave vector in order to reduce wrap-around errors and produce good energies respectively.

For the ZPL energy calculation, we use the constrained occupation DFT method.[39] The lowest energy optically excited state is calculated by promoting a Kohn-Sham particle from the highest occupied state to the lowest unoccupied state in the minority spin channel, see Figs. 1(b)–1(c). PBE can find the correct order for the ZPL energies of the non-equivalent configurations, but the absolute values are shifted down by 0.2–0.3 eV depending on the supercell size.[21] The ground state PBE wave functions are used to calculate the zero-field splitting (ZFS) tensor employing the implementation in VASP and the method presented in

Ref. 40. The latter method is called inhouse throughtout this paper. Both implementations calculate the spin-spin dipole interaction which is the first order approximation of the ZFS. Note that the latter implementation ignores the PAW contribution to the ZFS and produces good absolute values, while the implementation in VASP is formally more consistent.

The results of the HSE06 ground state calculations are post-processed to obtain the hyperfine field tensor[41] using the implementation present in VASP. This tensor describes the small energy splitting due to the interaction between the nuclear and electronic spin. Due to the higher natural abundance of the spin-1/2 ^{29}Si isotope (4.68%) than the spin-1/2 ^{13}C isotope (1.07%), it is easier to resolve the hyperfine signal of ^{29}Si in experiment. We calculate the hyperfine tensor of the second neighbor ^{29}Si nuclei sites for the divacancy. The different ^{29}Si nuclei sites are displayed in Fig. 1(d). For the silicon vacancy, the hyperfine tensors of ^{13}C for the silicon vacancy are calculated for the carbon atoms directly above the defect (C_1) and for the three carbon atoms below (C_2-C_4).

We also perform EPR experiments for the silicon vacancy in 6H-SiC at room temperature. The samples used for EPR experiments are high-purity semi-insulating 6H-SiC irradiated by 2-MeV electrons at room temperature followed by annealing at $400\,^\circ$C. The dose of irradiation was 8×10^{18} cm^{-2}. EPR measurements are performed on an X-band (9.4 GHz) spectrometer equipped with a He-flow cryostat, allowing the regulation of the sample temperature in the range of 4–295 K.

In this paper, a 1536 atom supercell ($8 \times 8 \times 2$) with basis vector lengths of 24.8 Å, 24.8 Å, and 30.4 Å is used. The size of the supercell together with Γ point sampling is sufficiently convergent for point defect configuration identification.[21,22] For the relative energy difference of the ZPL energy, we fitted a normal distribution with a standard deviation of 4.26 meV, which would correspond to a Full Width at Half Maximum (FWHM) of 10 meV. Here, we assume that 10 meV away from the calculated value, the probability of finding the correct ZPL drops to half. As it was discussed in Ref. 21 and evident from Fig. 2, a complete identification cannot be obtained from the ZPL results alone.

Figure 2(a) shows the calculated ZPL energies for the silicon vacancy. As can be seen in the figure, the theoretical ZPL lines for $k1$ and $k2$ overlap slightly, and hence, it is possible that these lines have a different order when compared to the experiments. The ZPL for the h site, however, has no overlap with other sites, and thus, the V1 center of the largest ZPL energy can be assigned to V_{Si} (-) at the h site.

In Fig. 2(b) for the divacancy ZPLs, the largest overlap is between $k1h$ and $k2k1$ also hh and $k1k1$; therefore, no assignment can be made directly. In contrast, since the ZPL lines for $k2k2$ do not overlap with
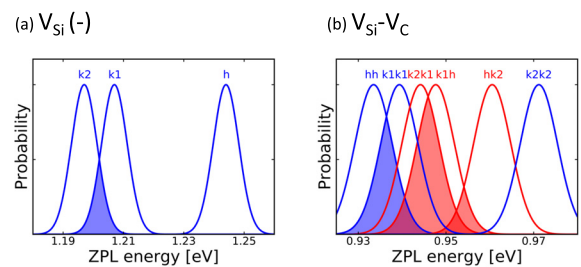

FIG. 2. Theoretical ZPL lines in 6H-SiC from DFT computations using the PBE functional. Estimated errors are depicted by Gaussians with a standard deviation of 4.2 meV. Shown are (a) the negatively charged silicon vacancy and (b) the neutral divacancy with the overlap filled in. Blue (red) color is for configurations with C_{3v} (C_{1h}) symmetry.

TABLE I. Theoretical and experimental magneto-optical data for divacancy configurations in 6H-SiC.

Configuration V_{Si}-V_C	Center[15,16]	ZPL (eV) Calc.	ZPL (eV) Exp.[16]	ZFS (GHz) Calc. (VASP)	ZFS (GHz) Calc. (inhouse)	ZFS (GHz) Exp.[16]
$k1k1$	QL1	0.939	1.088	1.494	1.300	1.300
hh	QL2	0.933	1.092	1.552	1.342	1.334
$k1h$	QL3	0.948	1.103	1.521	1.335	1.236
$k2k1$	QL4	0.944	1.119	1.549	1.343	…
$hk2$	QL5	0.961	1.134	1.559	1.355	1.383
$k2k2$	QL6	0.972	1.134	1.579	1.374	1.347

any other C_{3v} symmetric configurations, this configuration can be assigned to the highest energy divacancy related center, QL6. Note, also, that the order of $k1k1$ and $k2k1$ is clear when compared to the experimental data since they belong to different symmetry groups.

As divacancy defects have more applications, their results are discussed first. If one only use the PBE ZPL data presented in Table I for the divacancy, it suggests the following identification for QL1-QL6 in increasing order: hh, $k1k1$, $k2k1$, $k1h$, $hk2$, and $k2k2$. However, when the ZFS is also taken into account, one finds that a better agreement is given by reordering the identified configurations so that hh switches with $k1k1$ and $k2k1$ switches with $k1h$. As discussed above, hh and $k1k1$ as well as $k2k1$ and $k1h$ have a large overlap in the ZPL data, and this reordering gives better agreement with all the available data. Furthermore, taking the hyperfine splitting data in Table II into account further strengthens the decision to switch hh with $k1k1$. The final results of our identification are given in Table I.

In our identification, the C_{3v} configurations (hh, $k1k1$, and $k2k2$) are the most accurate given that all the data (ZPL, ZFS, and hyperfine) support this order. For the C_{1h} configurations ($hk2$, $k1h$, and $k2k1$), the results are consistent with the data presented here, but further hyperfine measurements are needed to verify the presented assignment of the configurations. In the supplementary material, additional hyperfine tensors are calculated to facilitate the interpretation of future experimental results. Additional experimental results would be especially useful for the $k1h$ and $k2k1$ configurations, where ZPL values have a large overlap and the ZFS value is missing for the $k2k1$ configuration. On the other hand, the $hk2$, which does not have a large overlap with $k1h$ and $k2k1$ in Fig. 2(b), is consistent with both the ZFS and

ZPL data. Note, also, that in the C_{1h} configurations, the spin-orbit interaction may contribute to the ZFS. As we only calculate the spin-spin dipolar contribution, we expect larger errors when the calculated ZFS is compared with the experimental values in these cases.

If one uses only the PBE ZPL data for the silicon vacancy, one would get an identification of V1-V3 centers in increasing order: $k2$, $k1$, and h. However, in similarity with the case for the divacancy, when one takes the ZFS results into account, the order of 2 adjacent configurations changes. In this case, the order changes between $k1$ and $k2$, as seen in Table III. Since the calculated ZFS is the smallest for the h site, 9.7 MHz from VASP and 3.7 MHz from the inhouse method, it matches well with the smallest experimental value of 13.3 MHz. The calculated largest ZFS value belongs to $k2$, 97.5 MHz and 97 MHz for the two computational techniques, respectively, which matches with the largest experimental value of 64.0 MHz. The ZFS of the $k1$ configuration does not fit the experimental value and thus does not aid the identification. Our EPR setup only measures the amplitude of the D-tensor. The ZFS results for the $k1$ and $k2$ configurations agree with the calculation and experiment done in Ref. 44, where the different signs of these configurations are explained.

Figure 3(a) shows an EPR spectrum in irradiated 6H-SiC measured at 292 K for the magnetic field along the c-axis ($\mathbf{B}||\mathbf{c}$). Here, the hyperfine structures due to the interaction between the electron spin and the nuclear spin of one ^{13}C occupying one of the four nearest neighbor C_1 (along the c-axis) and C_{2-4} (in basal plane) sites could be detected. However, the T_{V1a} and T_{V3a} signals could not be resolved, resulting in overlapping lines with a double intensity [see Fig. 3(a)]. Using smaller field modulation (0.6 G) and microwave (MW) power (0.6325 mW), the T_{V1a} and T_{V3a} lines and their hyperfine structures due to the interaction with one ^{29}Si occupying one of the 12 Si sites in the second neighbor can be observed, see Fig. 3(b). The fine-structure parameters D for these S = 3/2 centers are determined as 13.3 MHz for T_{V1a}, 64.0 MHz for T_{V2a}, and 13.9 MHz for T_{V3a}, see Table III. The isotropic Si_{II} hyperfine splittings for these centers are determined as 8.4 MHz for T_{V1a} and 8.1 MHz for T_{V2a} and T_{V3a}. Note that the fine-structure parameter for the h configuration reported in Ref. 44 is D = 0, whereas in our experiments, D = 13.3 MHz. In Ref. 44, the line-width of electron spin echo (ESE) is very broad (5 G full width at half maximum) and the $V_{Si}^-(h)$ line (i.e., T_{V1a}) and $V_{Si}^-(k1)$ line (i.e., T_{V3a}) cannot be resolved. The two observed doublets were assigned to $k1$ and $k2$ configurations, whereas h was assumed to have no ZFS with its low- and high-field lines coinciding with the central line.[44]

In Table IV, we compare the calculated principal values for the hyperfine tensors and the corresponding θ angles with the experimental data.[25] This tensor has values labeled A_{xx}, A_{yy}, and A_{zz} which

TABLE II. Theoretical and experimental hyperfine splitting for divacancy configurations in 6H-SiC for the C_{3v} symmetry configurations. The sites of the nuclei considered in the hyperfine calculations are marked in Fig. 1(d). The numbers in parentheses show the multiplicity of the sites. The hyperfine splitting (MHz) is A_z with correction.

Configuration V_{Si}-V_C	Center[15,16]	Si_{IIa} (3) Calc.	Si_{IIa} (3) Exp.[42]	Si_{IIb} (6) Calc.	Si_{IIb} (6) Exp.[42]
$k1k1$	QL1	12.70	12.7	9.46	10.0
hh	QL2	11.72	12.5	9.10	9.2
$k2k2$	QL6	11.72	13.3	9.23	9.2

TABLE III. Theoretical and experimental magneto-optical data for silicon vacancy configurations in 6H-SiC.

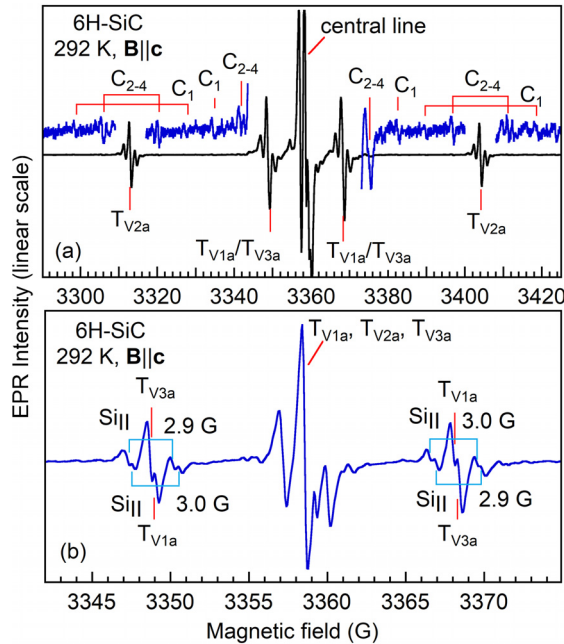| Configuration	Center[24]	ZPL (eV) Calc.	ZPL (eV) Exp.[43]	ZFS (MHz) Calc. (VASP)	ZFS (MHz) Calc. (inhouse)	ZFS (MHz) Exp. $|D_{exp}|$
$k1$	V3, T_{V3a}	1.207	1.368	−32.8	−26.7	13.9
$k2$	V2, T_{V2a}	1.197	1.398	97.5	97	64.0
h	V1, T_{V1a}	1.244	1.434	9.7	3.7	13.3

FIG. 3. (a) EPR spectra in electron-irradiated high-purity semi-insulating 6H-SiC measured at 292 K for **B**||**c** showing the low- and high-field lines and the central line of the negative Si vacancies T_{V1a}, T_{V2a}, and T_{V3a} as well as the C_1 and C_{2-4} hyperfine structures. With the modulation field of 0.7 G and the MW power of 1.262 mW, the signals of T_{V1a} and T_{V3a} are not resolved. (b) Using a modulation field of 0.6 G and a MW power of 0.6325 mW, the low- and high-field lines of T_{V1a} and T_{V3a} as well as their Si_{II} hyperfine structures could be resolved. The MW frequency is 9.415 GHz.

whereas A_{zz} is denoted as $A_\parallel$ with $\theta = 0$. These hyperfine data of the nearest neighboring C_1 and C_{2-4} of the Si vacancy were measured from the central line, which were considered to be related to the so-called no-ZFS negative Si vacancies V_{Si} (I) and V_{Si} (II).[25] The corresponding C_1 hyperfine data for the T_{V1a}, T_{V2a}, and T_{V3a} determined from our EPR experiments are also given. The C_1 and C_{2-4} hyperfine structures for the low- and high field lines of these centers are shown in Fig. 3(a). In Table IVa, the calculated $A_\perp$ and $A_\parallel$ for the C_1 nuclei for $k1$ and h are very close to those obtained from experiment and thus correspond to T_{V1a} and T_{V3a}. This conclusion is further strengthened by the 2 equal values reported in Ref. 25. In Table IVb, we compare the calculated results for A_{xx}, A_{yy}, and A_{zz} and the corresponding θ angle with the experimental data[25] for the C_{2-4} sites. Here, the presented experimental data also agree best with the $k1$ and h configurations. Due to the small angle difference between $k1$ and $k2$, it could be difficult to resolve the different amplitudes for these configurations.

When comparing the errors between the theoretical and experimental ZPL values in Table I and Table III, there is a fairly uniform systematic positive offset with an average magnitude of 0.15 eV for these configurations. The systematic error originates from the use of the PBE functional and has been thoroughly discussed in Ref. 21. Also, note that the ZFS values for the divacancy and silicon vacancy show notable differences in their relative accuracy when they are compared with experimental data. This can be explained by the difference in the absolute ZFS values and the absolute errors of the calculated ZFS values that are in the same order of magnitude for the two defects. Due to the dipolar interaction, all pairs of unpaired electron spin interact and give rise to a contribution to the total ZFS tensor. In the divacancy, there is only one unpaired electron spin pair which gives a ZFS contribution in the GHz range. However, in the silicon vacancy, there are three pairs of unpaired electron spins. Due to the high symmetry of the silicon vacancy (C_{3v}), the ZFS contributions cancel out to a large extent. Note that if the silicon vacancy would have T_d symmetry, the ZFS would be zero. On the other hand, such cancellation does not apply to the errors, thus explaining the larger relative errors for the silicon vacancy.

correspond to the $[1\bar{1}00]$, $[11\bar{2}0]$, and $[0001]$-direction, and θ is the angle to the $[0001]$-direction [cf. Fig. 1(c) in Ref. 25, where the same values are denoted A_x, A_y, and A_z]. For nuclei in high symmetric positions, such as C_1, $A_{xx} = A_{yy}$ and thus denoted as $A_\perp$ with $\theta = 90$,

TABLE IV. Theoretical and experimental hyperfine splitting (MHz) for silicon vacancy configurations in 6H-SiC for the nuclei site (a) C_1 and sites (b) C_{2-4} is presented with the same labeling as in Ref. 25.

(a) The parallel and perpendicular components are presented from our calculation and measurements, and from Ref. 25.

Configuration	Center[24,25]	Calc.		Exp.		Exp.[25]	
		$A_\parallel$	$A_\perp$	$A_\parallel$	$A_\perp$	$A_\parallel$	$A_\perp$
$k1$	T_{V3a}, V_{Si}^-(I)	84.3	30.3	80.5	33.6	80.0	32.8
$k2$	T_{V2a}	83.3	33.2	80.5	33.0	…	…
h	T_{V1a}, V_{Si}^-(II)	84.6	31.2	80.5	33.6	80.0	32.8

(b) For the three degenerate C_{2-4} sites, the A_{xx}, A_{yy}, and A_{zz} components with their corresponding θ value are presented and compared.

Configuration	Center[24,25]	Calc.			Exp.[25]		
		$A_{xx}(\theta)$	$A_{yy}(90)$	$A_{zz}(\theta)$	$A_{xx}(\theta)$	$A_{yy}(90)$	$A_{zz}(\theta)$
$k1$	T_{V3a}, V_{Si}^-(I)	79.9(109.7)	26.6	27.0(19.7)	75.8(110.0)	28.4	28.2(20.0)
$k2$	T_{V2a}	85.3(109.6)	30.8	30.8(19.6)	…	…	…
h	T_{V1a}, V_{Si}^-(II)	83.6(108.9)	30.1	30.1(18.9)	80.3(109.1)	31.6	31.4(19.1)

To conclude, in this paper, we have provided an identification of two common point defects in 6H-SiC: the negatively charged silicon vacancy and neutral divacancy. Our identification was done by comparing ZPL, ZFS, and hyperfine data from both theoretical calculations and experiments. The 3 different configurations for the negatively charged silicon vacancy are $k1$, $k2$, and h which have the following experimental ZPL of 1.368, 1.398, and 1.434 eV, respectively. For the six divacancy configurations, we identify the three C_{3v} symmetry configurations $k1k1$, hh, and $k2k2$ with experimental ZPL of 1.088, 1.092, and 1.134 eV, respectively. Finally, for the three configurations with C_{1h} symmetry $k1h$, $k2k1$, and $hk2$, we obtain 1.103, 1.119, and 1.134 eV. Our results explain the defect configurations seen in recent experiments and may aid future work on defect engineering in SiC for quantum technologies.

No experimental hyperfine data are available yet for one of the silicon vacancy configurations and for the C_{1h} symmetry configurations in the divacancy. Once experimental data are available, they can be compared with the theoretically calculated hyperfine tensors presented in the supplementary material and be used to further support the identification presented in this paper.

See supplementary material for additional hyperfine splitting tensors for the silicon vacancy and divacancy.

REFERENCES

[1] F. Jelezko and J. Wrachtrup, Phys. Status Solidi A **203**, 3207 (2006).

[2] R. Hanson and D. D. Awschalom, Nature (London) **453**, 1043 (2008).

[3] D. D. Awschalom, L. C. Bassett, A. S. Dzurak, E. L. Hu, and J. R. Petta, Science **339**, 1174 (2013).

[4] L. Childress, J. M. Taylor, A. S. Sørensen, and M. D. Lukin, Phys. Rev. Lett. **96**, 070504 (2006).

[5] I. Aharonovich, S. Castelletto, D. A. Simpson, A. Stacey, J. McCallum, A. D. Greentree, and S. Prawer, Nano Lett. **9**, 3191 (2009).

[6] R. Kolesov, K. Xia, R. Reuter, R. Stöhr, A. Zappe, J. Meijer, P. R. Hemmer, and J. Wrachtrup, Nat. Commun. **3**, 1029 (2012).

[7] S. Castelletto, B. C. Johnson, V. Ivády, N. Stavrias, T. Umeda, A. Gali, and T. Ohshima, Nat. Mater. **13**, 151 (2014).

[8] I. Aharonovich, D. Englund, and Milos Toth, Nat. Photonics **10**, 631 (2016).

[9] J. R. Weber, W. F. Koehl, J. B. Varley, A. Janotti, B. B. Buckley, C. G. Van de Walle, and D. D. Awschalom, Proc. Natl. Acad. Sci. **107**, 8513 (2010).

[10] J. Wrachtrup and F. Jelezko, J. Phys.-Condens. Matter **18**, S807 (2006).

[11] G. Kucsko, P. C. Maurer, N. Y. Yao, M. Kubo, H. J. Noh, P. K. Lo, H. Park, and M. D. Lukin, Nature **500**, 54 EP (2013).

[12] A. L. Falk, P. V. Klimov, B. B. Buckley, V. Ivády, I. A. Abrikosov, G. Calusine, W. F. Koehl, A. Gali, and D. D. Awschalom, Phys. Rev. Lett. **112**, 187601 (2014).

[13] G. Balasubramanian, I. Y. Chan, R. Kolesov, M. Al-Hmoud, J. Tisler, C. Shin, C. Kim, A. Wojcik, P. R. Hemmer, A. Krueger, T. Hanke, A. Leitenstorfer, R. Bratschitsch, F. Jelezko, and J. Wrachtrup, Nature **455**, 648 (2008).

[14] M. W. Doherty, N. B. Manson, P. Delaney, F. Jelezko, J. Wrachtrup, and L. C. Hollenberg, "The nitrogen-vacancy colour centre in diamond," Phys. Rep. **528**, 1 (2013).

[15] W. F. Koehl, B. B. Buckley, F. J. Heremans, G. Calusine, and D. D. Awschalom, Nature **479**, 84 (2011).

[16] A. L. Falk, B. B. Buckley, G. Calusine, W. F. Koehl, V. V. Dobrovitski, A. Politi, C. A. Zorman, P. X.-L. Feng, and D. D. Awschalom, Nat. Commun. **4**, 1819 (2013).

[17] V. A. Soltamov, A. A. Soltamova, P. G. Baranov, and I. I. Proskuryakov, Phys. Rev. Lett. **108**, 226402 (2012).

[18] M. Widmann, S.-Y. Lee, T. Rendler, N. T. Son, H. Fedder, S. Paik, L.-P. Yang, N. Zhao, S. Yang, I. Booker, A. Denisenko, M. Jamali, S. A. Momenzadeh, I. Gerhardt, T. Ohshima, A. Gali, E. Janzén, and J. Wrachtrup, Nat. Mater. **14**, 164 (2015).

[19] G. Balasubramanian, P. Neumann, D. Twitchen, M. Markham, R. Kolesov, N. Mizuochi, J. Isoya, J. Achard, J. Beck, J. Tissler, V. Jacques, P. R. Hemmer, F. Jelezko, and J. Wrachtrup, Nat. Mater. **8**, 383 (2009).

[20] D. J. Christle, A. L. Falk, P. Andrich, P. V. Klimov, J. U. Hassan, N. T. Son, E. Janzén, T. Ohshima, and D. D. Awschalom, Nat. Mater. **14**, 160 (2015).

[21] J. Davidsson, V. Ivdy, R. Armiento, N. T. Son, A. Gali, and I. A. Abrikosov, New J. Phys. **20**, 023035 (2018).

[22] V. Ivády, J. Davidsson, N. T. Son, T. Ohshima, I. A. Abrikosov, and A. Gali, Phys. Rev. B **96**, 161114 (2017).

[23] L. Gordon, A. Janotti, and C. G. Van de Walle, Phys. Rev. B **92**, 045208 (2015).

[24] E. Sörman, N. T. Son, W. Chen, O. Kordina, C. Hallin, and E. Janzén, Phys. Rev. B **61**, 2613 (2000).

[25] N. Mizuochi, S. Yamasaki, H. Takizawa, N. Morishita, T. Ohshima, H. Itoh, and J. Isoya, Phys. Rev. B **68**, 165206 (2003).

[26] P. G. Baranov, I. Ilin, E. Mokhov, M. Muzafarova, S. B. Orlinskii, and J. Schmidt, J. Exp. Theor. Phys. Lett. **82**, 441 (2005).

[27] N. T. Son, P. Carlsson, J. ul Hassan, E. Janzén, T. Umeda, J. Isoya, A. Gali, M. Bockstedte, N. Morishita, T. Ohshima, and H. Itoh, Phys. Rev. Lett. **96**, 055501 (2006).

[28] Ö. Soykal, P. Dev, and S. E. Economou, Phys. Rev. B **93**, 081207 (2016).

[29] P. Hohenberg and W. Kohn, Phys. Rev. **136**, B864 (1964).

[30] W. Kohn and L. J. Sham, Phys. Rev. **140**, A1133 (1965).

[31] V. Ivády, I. A. Abrikosov, and A. Gali, NPJ Comput. Mater. **4**, 76 (2018).

[32] G. Kresse and J. Hafner, Phys. Rev. B **49**, 14251 (1994).

[33] G. Kresse and J. Furthmüller, Phys. Rev. B **54**, 11169 (1996).

[34] P. E. Blöchl, Phys. Rev. B **50**, 17953 (1994).

[35] G. Kresse and D. Joubert, Phys. Rev. B **59**, 1758 (1999).

[36] J. P. Perdew, K. Burke, and M. Ernzerhof, Phys. Rev. Lett. **77**, 3865 (1996).

[37] J. Heyd, G. E. Scuseria, and M. Ernzerhof, J. Chem. Phys. **118**, 8207 (2003).

[38] J. Heyd, G. E. Scuseria, and M. Ernzerhof, J. Chem. Phys. **124**, 219906 (2006).

[39] A. Gali, E. Janzén, P. Deák, G. Kresse, and E. Kaxiras, Phys. Rev. Lett. **103**, 186404 (2009).

[40] V. Ivády, T. Simon, J. R. Maze, I. A. Abrikosov, and A. Gali, Phys. Rev. B **90**, 235205 (2014).

[41] K. Szász, T. Hornos, M. Marsman, and A. Gali, Phys. Rev. B **88**, 075202 (2013).

[42] A. L. Falk, P. V. Klimov, V. Ivády, K. Szász, D. J. Christle, W. F. Koehl, A. Gali, and D. D. Awschalom, Phys. Rev. Lett. **114**, 247603 (2015).

[43] E. Janzén and B. Magnusson, in *Silicon Carbide and Related Materials 2004*, Materials Science Forum (Trans Tech Publications, 2005), Vol. 483, pp. 341–346.

[44] T. Biktagirov, W. G. Schmidt, U. Gerstmann, B. Yavkin, S. Orlinskii, P. Baranov, V. Dyakonov, and V. Soltamov, Phys. Rev. B **98**, 195204 (2018).